ACS APPLIED MATERIALS & INTERFACES

www.acsami.org

Research Article

Interfacial Engineering of Hybrid Polydopamine/Polypyrrole Nanosheets with Narrow Band Gaps for Fluorescence Sensing of MicroRNA

Mengnan Yang, Zhenqiang Wang, Tao Ding, Jia Tang, Xiyue Xie, Yuxin Xing, Lu Wang,* Jixi Zhang,* and Kaiyong Cai

Cite This: https://doi.org/10.1021/acsami.1c11301

Read Online

ACCESS | Metrics & More | Article Recommendations | Supporting Information

ABSTRACT: Nanoquencher-based biosensors have emerged as powerful tools for the detection of tumor markers, where challenges in efficiently docking the π-electron interaction interface toward nucleic acid probes containing π-electron-rich units of bases and fluorescent dyes still remain. Herein, we present hybrid polydopamine/polypyrrole nanosheets (PDA-PPy-NS) with π electron coupling and ultranarrow band gap (0.29 eV) by interfacial engineering of polymer hybrids at the nanoscale. PDA-PPy-NS were first prepared through oxidant-induced polymerization of pyrrole on PDA nanosheets. By utilizing fluorescent-dye-labeled single-stranded DNA as a probe, the hybrid nanoquencher showed ultrahigh fluorescence quenching ability, i.e., a Cy5-ssDNA/nanoquencher mass ratio of 36.9 under the complete quenching condition, which is comparable to that of graphene oxide. It was demonstrated that the energy level coupling of nanosheets and nucleic acid dye (Cy5) was the key factor contributing to the efficient photoinduced electron transfer (PET). Subsequently, the nanoquencher/DNA probe was proved to possess superior sensitivity and selectivity for efficient and reliable detection of miRNA-21 with a detection limit of 23.1 pM. Our work proves that the π-electron-rich biosensor interface can significantly enhance the PET efficiency, providing a theoretical basis for developing novel high-performance sensors.

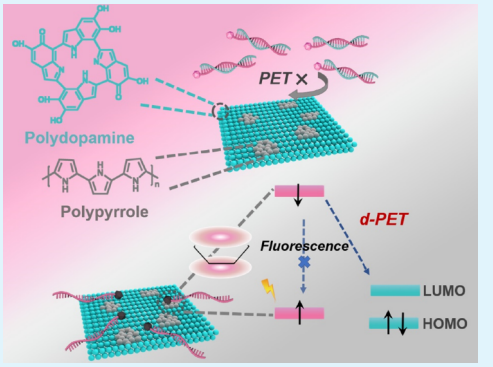

KEYWORDS: *fluorescent nanoquencher, π-conjugated structure, energy level coupling, interfacial electron transfer, nucleic acid sensing*

1. INTRODUCTION

As a representative of new tumor biomarkers, microRNA (miRNA) is a class of noncoding small molecular RNA with a length of about 21 nucleotides.[1,2] Its accurate detection is of great significance for auxiliary diagnosis and prognosis evaluation.[3] Among various explorations of miRNA detection methods, fluorescence sensor systems show advanced features of simplicity and convenience in controlling the switching-on of the detection function and the change in optical signals, by combining the advantages of high specific molecular recognition of nucleic acid nanotechnology, nonradiative transition-inducing capacities of nanomaterials (fluorescent nanoquenchers), and the adaptive behaviors (binding, recognition, hybridization, release, etc.) of nucleic acid probes.[4−6] In a complex and dynamic physiological environment, the detection properties are highly dependent on the interfacial interactions and electron/energy transfer, and it is a great challenge to effectively suppress the background interference by rational design and optimization of the nanoquenchers.[7,8]

From a molecular structure point of view, nucleic acid probes are biological macromolecules containing π-electron-rich units including bases and fluorescent dyes.[9] Therefore, fluorescence quenching and sensing systems can be readily achieved based on π-electron coupling through $\pi-\pi$ stacking and π-cation interactions.[5] Organic semiconductor nanomaterials with π-conjugated structures can efficiently dock the π-electron interaction interface and bring new opportunities for solving the above problems.[10,11] From the perspective of material construction, conjugated polymers with narrow band gaps can promote more delocalized π electrons and more efficient charge separation, which is a necessary condition for achieving intermolecular electron coupling, promoting efficient fluorescence quenching and miRNA responses.[12]

The narrow band gap semiconductor polymer materials with adjustable energy levels can be obtained through the technical strategies of structural modifications by molecular engineering.[13] However, at the nanoscale, conjugated polymer systems are assembled through complex and variable noncovalent

Received: June 17, 2021
Accepted: August 14, 2021

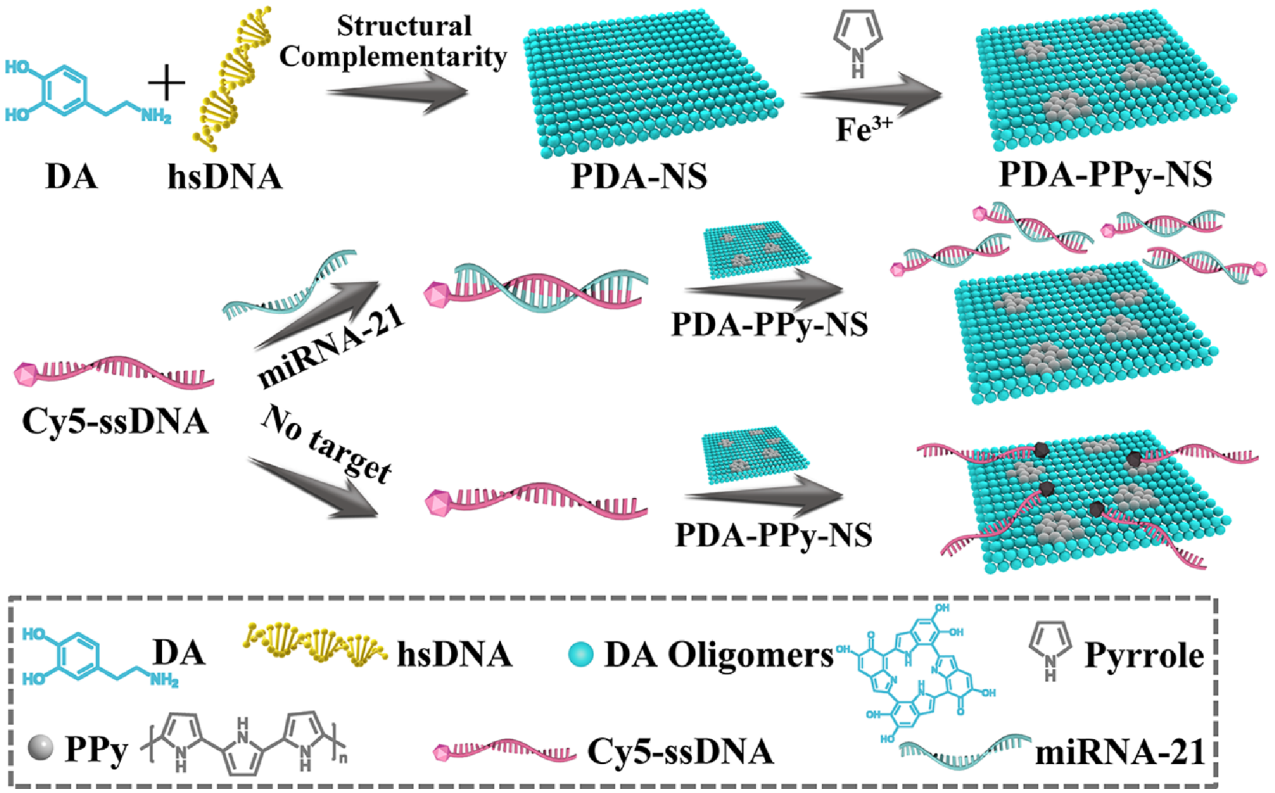

Figure 1. Schematic representation of the Cy5-ssDNA/PDA-PPy-NS-based sensing nanoplatform.

interactions to form aggregation states with different microstructures.[14] As a result, the carrier transport process, energy levels/band gaps, and other semiconductor properties are significantly influenced by the stacking parameters of conjugated elements at the molecular scale, the aggregation behavior at the nanoscale, and the self-assembly process.[14,15] However, the lowest band gap of the energy-level-engineered nanoparticles is only in the range of 0.9−1.5 eV.[16,17] Moreover, while fewer studies focused on the applications in nanoquenchers, most of the narrow band gap nanomaterials were applied as robust photoacoustic imaging and photothermal treatment agents because of their high efficiency in mediating another type of nonradiative transition process, i.e., photothermal conversion. In contrast, the doping and hybridization of materials at the molecular scale and nanoscale, as well as the regulation of the optical band gap, can be achieved through interface engineering and band engineering.[18,19] Two-dimensional semiconducting nanostructures, especially heterojunction-based nanostructures, are quite appealing in inducing significant intralayer quantum confinement and interlayer unit synergy effects, which can facilitate efficient photoinduced electron transfer (PET) for fluorescence sensing.[20]

Herein, we reported the proof-of-concept design of a two-dimensional nanoquencher with π electron coupling and narrow band gaps for fluorescence sensing of miRNA (Figure 1). Specifically, a substrate material from our previous studies, i.e., DNA-directed polydopamine nanosheets (PDA-NS) with vertically interdigitated and laterally packed primary planar structures,[21] was employed for building the hybrid nanoquencher. Pyrrole (Py) monomers were subsequently accommodated and hybridized on the nanosheets through $\pi-\pi$ stacking of conjugated units and oxidant-induced polymerization ($FeCl_3$). Varying ratios of Py/PDA-NS (w/w, 0.39, 0.68, and 0.97) were designed to tune the band gaps of the obtained nanosheets (polydopamine/polypyrrole nanosheets (PDA-PPy-NS)). The photophysical properties of the nanosheets and the fluorescence quenching capacities toward fluorescently labeled DNA probes (Cy5-ssDNA) were analyzed to demonstrate the impact of greatly enhanced PET generated by the structural design. Then, based on the affinity difference of the PDA two-dimensional nanoquencher toward double-stranded (ds) and single-stranded (ss) nucleic acids, a fluorescence sensing platform was successfully constructed for miRNA quantitative analysis. The great potential of the hybrid nanoquencher was illustrated by the miRNA detection properties.

2. EXPERIMENTAL SECTION

2.1. Materials and Reagents. Unless otherwise indicated, all reagent-grade chemicals were used as received and distilled water was used to prepare all aqueous solutions. Deoxyribonucleic acid of herring sperm (hsDNA, with base lengths below 150 bp and averaged at around 50 bp) was purchased from Solarbio Science & Technology Co., Ltd (Beijing, China). Dopamine hydrochloride (AR, 98%), tris(hydroxymethyl)aminomethane (Tris, 99.9%), tetrahydrofuran, and phosphate-buffered saline (PBS, pH 7.4) were purchased from Aladdin Industrial, Inc. Pyrrole (Py) was purchased from Macklin (Shanghai, China). Iron(III) chloride anhydrous ($FeCl_3$) was purchased from Alfa Aesar. Pluronic F127 was purchased from Sigma (Shanghai, China). Ethanol (AR) was purchased from Fluka. RNase inhibitor and diethyl pyrocarbonate-treated water were purchased from Takara Biotechnology Co., Ltd (Dalian, China). Tetrabutylammonium hexafluorophosphate (TBAPF6) was purchased from Adamas. DNA/miRNA sequences were synthesized and purified by TSINGKE Biotechnology Co., Ltd (Beijing, China) and Takara Biotechnology (Dalian, China), respectively. Sequences of oligonucleotides are listed in Table S1. A total-RNA extraction kit was purchased from TiaGen Biotechnology Co., Ltd.

https://doi.org/10.1021/acsami.1c11301
ACS Appl. Mater. Interfaces XXXX, XXX, XXX−XXX

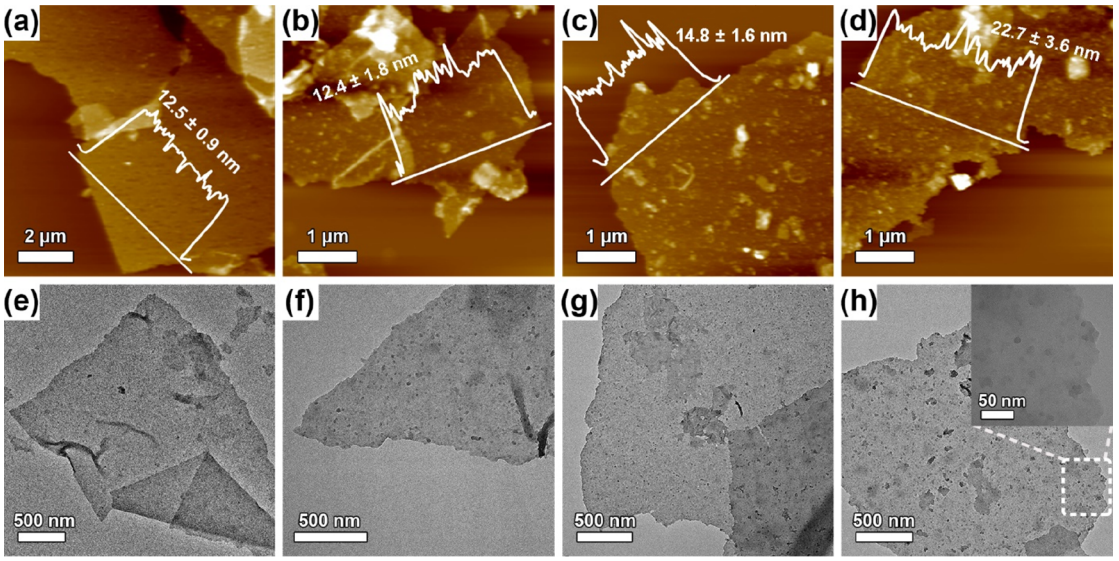

Figure 2. Morphology characterizations of nanosheets: AFM (the substrate: mica sheet; insets: height distributions) and TEM images of (a and e) PDA-NS, (b and f) PDA-PPy-0.39-NS, (c and g) PDA-PPy-0.68-NS, and (d and h) PDA-PPy-0.97-NS; inset: enlarged TEM image of the selected region from (h).

2.2. Synthesis of PDA Nanosheets and PDA-PPy Nanosheets. PDA-NS were prepared by the DNA soft template method reported by our group.[21] Briefly, hsDNA and dopamine hydrochloride at a mass ratio of 1:1 were added into a Tris solution (2.6 mg mL^{-1}) and stirred at room temperature for 24 h. The suspension was then centrifuged at 11 000 rpm for 10 min and washed twice with distilled water to obtain the products.

PDA-PPy-NS were successfully prepared by in situ polymerization of Py monomers on PDA-NS via $\pi-\pi$ stacking and oxidant (Fe^{3+}) induction. First, various amounts of Py (2, 3.5, and 5 μL) monomers were added into 1.75 mL of deionized water containing PDA-NS (5 mg). The reaction mixture was stirred at room temperature for 24 h to adsorb Py onto the nanosheets. Afterward, 0.25 mL of $FeCl_3$ aqueous solution (24, 42, and 60 mg mL^{-1}) was added into the PDA-NS suspension together with Py to initiate the polymerization of the Py monomers. After vigorously stirring for another 2 h, Py was polymerized into PPy and firmly adhered to the surface of the PDA and DNA structures. The suspension was then centrifuged at 11 000 rpm for 8 min and washed twice with distilled water to remove impurities. Finally, the deposition of nanosheets was dispersed in distilled water and stored at 4 °C for further use. The resulting nanosheets were denoted as PDA-PPy-*x*-NS, where *x* represents the mass ratios of Py/PDA-NS (0.39, 0.68, and 0.97). PPy nanoparticles were prepared by an oxidant (Fe^{3+})-induced polymerization in the absence of PDA-NS, and F127 was used as a stabilizer.[22]

Experimental details on the morphology, composition, and structure analysis of the nanosheets, optical/electrochemical properties, band gap/energy level calculations, and fluorescence spectra measurements are included in the Supporting Information.

2.3. Fluorescence Quenching Studies. All experiments were performed in PBS buffer (120 mM NaCl, 10 mM $MgCl_2$, pH 7.4). First, fluorescence quenching kinetics analysis was performed. The targets (miRNA-21, 50 nM) and fluorescent probes entirely complementary to the target sequence (ssDNA, 50 nM) were hybridized for 60 min at 37 °C in the PBS buffer to obtain ssDNA/miRNA heteroduplexes (dsDNA). The fluorescence signal intensity of dsDNA and ssDNA at 665 nm was recorded every 3 s at an excitation wavelength of 645 nm after the addition of NS (10 μg mL^{-1}).

To investigate the optimal quenching concentration of nanosheets, the Cy5-labeled ssDNA probes (50 nM) were mixed with different concentrations of nanosheets in a total volume of 600 μL. The mixtures were subsequently incubated at 37 °C for 30 min. The fluorescence signals of the samples were collected by using an RF-6000 fluorescence spectrophotometer (Shimadzu, Japan).

2.4. miRNA-21 Detection Performance. To optimize the detection parameters in the sensing application, the ratio (F/F_0) of fluorescence for suspensions of the nanoquencher (10 μg mL^{-1}) and probe (50 nM) in the presence/absence of 100 nM miRNA was detected and compared at varying temperatures (20, 30, 37, 45, and 55 °C), pH values (5.5, 6.5, 7.4, and 8.5), and salt concentrations (40, 60, 80, 100, and 120 mM of NaCl in the PBS buffer).

In a typical detection assay, miRNA-21 with various concentrations (0.005, 0.01, 0.02, 0.05, 0.1, 0.2, 0.5, 1, 2.5, 5, 10, 15, 25, 50, and 100 nM) was added into 50 nM Cy5-labeled ssDNA probes in the PBS buffer. The mixtures were allowed to react for 60 min at 37 °C to form heterologous DNA−miRNA double strands. Then, PDA-NS (40 μg mL^{-1}) or PDA-NS-PPy (10 μg mL^{-1}) was added into the above solution to make a total volume of 600 μL. After incubation at 37 °C for 30 min, the fluorescence spectra in the range of 657−750 nm were recorded. In addition to miRNA-21 (100 nM), single-base mismatched miRNA-21 (SM-miR-21), double-base mismatched miRNA-21 (DM-miR-21), three-base mismatched miRNA-21 (TM-miR-21), and two other miRNAs (miRNA-141 and let-7a) were used as controls under the same conditions to evaluate the selectivity of the constructed detection system.

Samples through adding different amounts of miRNA-21 (final concentration: 0.1, 0.05, and 0.01 nM) in fetal bovine serum (10 vol % in PBS, pH 7.4) were used to realize the simulation of biological samples. The analytical recoveries were calculated by using the standard curve. Additionally, total RNA samples of cell lysate for a tumor cell line (MCF-7 with a high abundance of upregulated miRNA-21) were also employed to investigate the application potential of the nanosensors in the detection of realistic biological samples. The cultured cells were processed with cell counting to obtain samples with different amounts of cells (10^4-10^8 cells). The total RNA of cells was extracted according to the manufacturer's protocol. Finally, the total RNA solutions were prepared in PBS and stored at −20 °C for further detection experiments.

3. RESULTS AND DISCUSSION

PDA-NS and PDA-PPy-NS were first fabricated by the strategies of DNA-directed assembly/growth of PDA[21] and oxidation-induced interfacial polymerization/hybridization of PPy,[23] respectively. The morphological analyses of the prepared PDA-NS and PDA-PPy-NS were performed by atomic force microscopy (AFM) and transmission electron microscopy (TEM) measurements. Both AFM and TEM

https://doi.org/10.1021/acsami.1c11301
ACS Appl. Mater. Interfaces XXXX, XXX, XXX−XXX

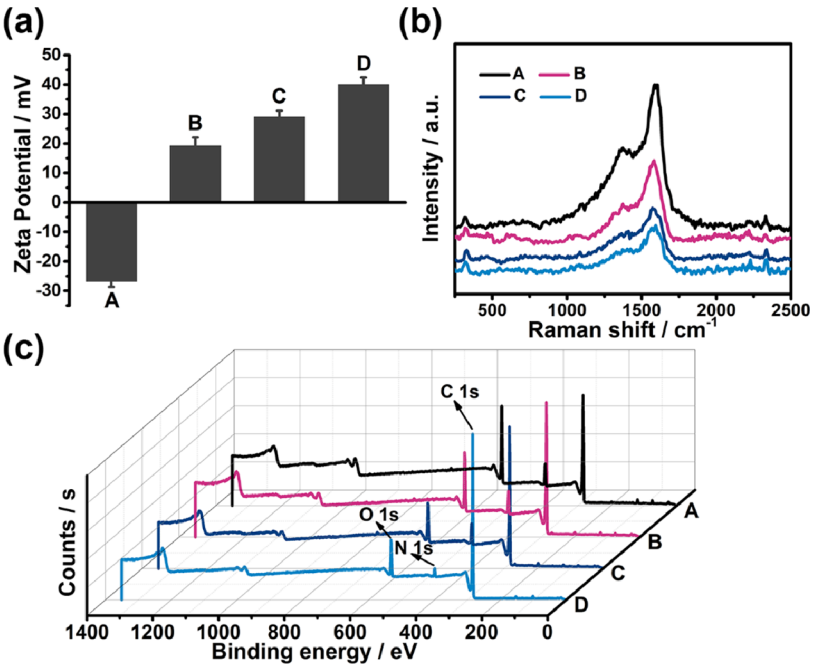

Figure 3. Composition characterizations of nanosheets: (a) zeta potentials, (b) Raman spectra, and (c) XPS spectra. Error bar in (a) represents the standard deviation of three independent measurements. (A)−(D) show PDA-NS, PDA-PPy-0.39-NS, PDA-PPy-0.58-NS, and PDA-PPy-0.97-NS, respectively.

images clearly reveal that all nanosheets have lateral sizes up to several micrometers with various thicknesses and stacked folds (Figure 2a−h). While barely changed at a lower Py/PDA-NS weight ratio (0.39) (∼12.4 nm, Figure 2b), the thickness of PDA-PPy-NS did increase to 14.8 ± 1.6 nm (Figure 2c) and 22.7 ± 3.6 nm (Figure 2d) when Py/PDA-NS weight ratios reached 0.68 and 0.97, respectively. Meanwhile, the surface roughness increased from ∼4 to ∼7 and ∼13 nm, respectively (Figure S1). Notably, some small black dots on the surface of PDA-PPy-NS can be clearly observed in TEM images (10−20 nm, Figure 2e−h), confirming the successful surface modification with polypyrrole (PPy). TEM images also show that in the absence of PDA-NS, most PPy nanoparticles are highly hydrophobic and tend to aggregate in an aqueous environment (Figure S2).

As shown in Figure 3a, the zeta potential of nanosheets was found to increase along with the addition of positively charged PPy. Furthermore, in agreement with previous studies,[23,24] due to the existence of a similar five-membered heterocyclic ring with a nitrogen atom in the 5,6-dihydroxyindole unit of PDA and the molecular structure of PPy, the Raman spectra of PDA-PPy-NS do not show any new peaks, compared with PDA-NS (Figure 3b). Composition analysis, carried out by X-ray photoelectron spectroscopy (XPS, Figure 3c), depicted gradually reduced O/C atomic ratios from 0.32 (PDA-NS) to 0.22, 0.16, and 0.12 (PDA-PPy-NS) with an increase in the mass ratios of Py/PDA-NS. Considering the absence of oxygen atoms in the molecular structure of PPy, the mass percentages of oxygen before and after PPy hybridization were employed to estimate the PPy weight percentages in PDA-PPy-NS, and the calculated values were 24%, 40%, and 50%, respectively.

The band structures and physical properties of nanosheets were then examined by a combination of photophysical and electrochemical analyses. As the doping level of PPy increased, the absorption spectra of PDA-PPy-NS displayed an intense increase at the wavelength of 600−900 nm (Figure 4a), which was attributed to the characteristic absorption of PPy. The absorbance of nanosheets showed a good linear correlation with the concentration at 665 nm. Accordingly, the extinction coefficient of nanosheets at 665 nm (ε) gradually increased from 5.85 to 8.15, 9.63, and 10.55 L g^{-1} cm^{-1} (Figure 4b). Changes in photophysical properties of PDA-PPy-NS may be ascribed to the changes in energy levels and band gaps. To verify this, the optical band gaps of nanosheet solid powder were obtained by the UV−vis−NIR absorption spectra and diffuse reflectance spectra (DRS) at 200 nm−1.5 μm. The results showed that the absorption onset values of PDA-NS and PDA-PPy-0.97-NS determined by the tangent lines in DRS[25−27] were 1722/4320 nm, corresponding to a band gap of 0.72/0.29 eV (Figure 4c,d). Notably, the ultranarrow band gap is even remarkably lower than the values obtained from previous systems using silica nanoparticles (2.32 eV)[19] or mesoporous PDA nanoparticles (0.56 eV)[23] as templates for the interfacial construction of PDA−PPy hybrids. This great success in narrowing down the band gap should be attributed to the employment of PDA nanosheets with a high surface-to-volume ratio to facilitate large-area heterojunctions of PDA−PPy. The band gap of nanosheets remained substantially unchanged when Py/PDA-NS weight ratios reached 0.97; therefore, PDA-PPy-0.97-NS were selected for the following studies on electrochemical properties and the mechanism of fluorescence quenching. Furthermore, the oxidation potentials (E_{ox}) of semiconductors were 0.372 V (PDA-NS) and 0.642 V (PDA-PPy-0.97-NS), obtained from the cyclic voltammetry (CV) curves (Figure 4e). Based on this, the lowest molecular occupied orbital (LUMO) and the highest molecular occupied orbital (HOMO) of PDA-NS and PDA-PPy-0.97-NS were thereby calculated as −4.04/−4.76 eV and −4.74/−5.03 eV (Figure 4f).

Moreover, Mott−Schottky (MS) curves of nanosheets were collected, and slopes for both PDA-NS and PDA-PPy-0.97-NS were positive (Figure 5a), indicating that they were all n-type

https://doi.org/10.1021/acsami.1c11301
ACS Appl. Mater. Interfaces XXXX, XXX, XXX−XXX

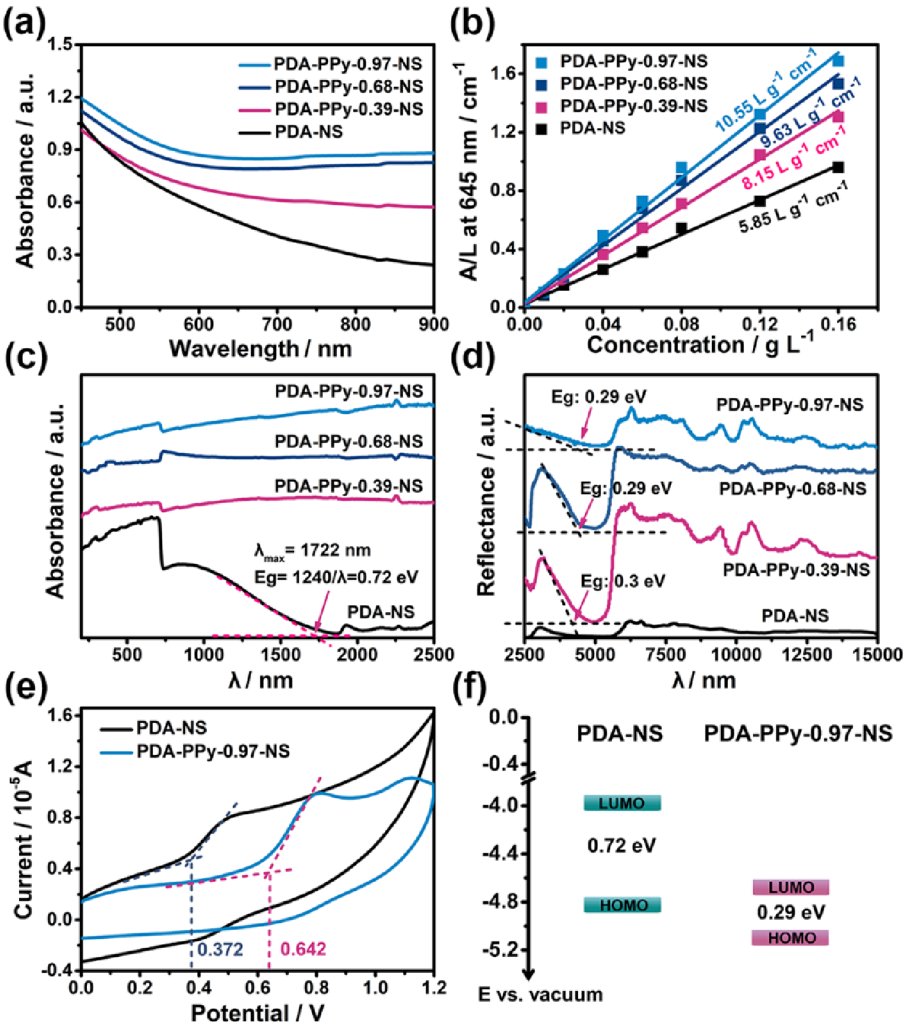

Figure 4. Photophysical and electrochemical properties of nanosheets: (a) UV−vis−NIR absorption spectra of nanosheets (60 μg mL^{-1}) in aqueous solution; (b) extinction coefficient at 665 nm; (c) UV−vis−NIR absorption spectra and (d) DRS with corresponding band gap energy calculations for nanosheet solid powders; (e) CV plots; and (f) diagram of the energy band structure.

semiconductors.[28,29] It is also of note that PDA-PPy-0.97-NS showed a smaller slope in the quasi-linear region of the MS plot, indicating a higher carrier density that is in correlation with the charge separation.[30,31] The electrochemical impedance spectra (EIS) in Figure 5b show that the PDA-PPy-0.97-NS possessed smaller resistance than PDA-NS, implying that PDA-PPy-0.97-NS displayed higher conductivity, which could, in turn, ensure faster electron transfer. Compared to PDA-NS, the electron paramagnetic resonance (EPR) spectrum of PDA-PPy-0.97-NS exhibited a stronger signal with some slight shifts relative to PPy, demonstrating the presence of unpaired electrons due to the π electron delocalization between PPy and PDA (Figure 5c). Through enhancement of intramolecular and intermolecular interactions, π electron delocalization has been found to be propitious to interfacial electron transfer.[32]

To evaluate the potential of PDA-PPy-NS as a nano-quencher of nucleic acids, the fluorescent dye Cy5 was introduced to label the ssDNA probe. UV−vis absorption spectra of Cy5-ssDNA with various concentrations (0−50 μg mL^{-1}) of PDA-PPy-0.97-NS showed that the absorption intensity increased gradually and possessed a characteristic absorption peak approximately at 645 nm (Figure S3a). Further increasing the PDA-PPy-0.97-NS concentration resulted in a red shift of the peak, indicating the formation of a ground-state complex[33] between Cy5-ssDNA and PDA-PPy-0.97-NS. Meanwhile, fluorescence intensities of 250 nM Cy5-ssDNA were efficiently quenched after the addition of PDA-PPy-0.97-NS (Figure S3b). Evidently, this significant fluorescence quenching revealed a strong interaction between the excited state of Cy5-ssDNA and PDA-PPy-0.97-NS. The deactivation of the excited state Cy5 could be attributed to PET efficiency and/or fluorescence resonance energy transfer.[34,35]

Subsequently, we investigated the mechanism of fluorescence quenching between Cy5 and PDA-PPy-0.97-NS by using fs-ultrafast transient absorption spectra (TAS). As shown in Figure 6a, the 2D map of TAS for Cy5/PDA-PPy-0.97-NS complexes was changed from 0 to 7.3 ns in the wavelength region of 615−740 nm. The 2D plots of the samples provide information on the transient absorption intensity and dynamic response range by color variation and the vertical span. Lower ΔA (transient absorption signals) values of the spectra for Cy5/PDA-PPy-0.97-NS complexes may be ascribed to the absorption of the nanosheets themselves and the quenching of the excited state over the laser pulse, which was also observed in previous studies on TAS of suspensions containing light-

https://doi.org/10.1021/acsami.1c11301
ACS Appl. Mater. Interfaces XXXX, XXX, XXX−XXX

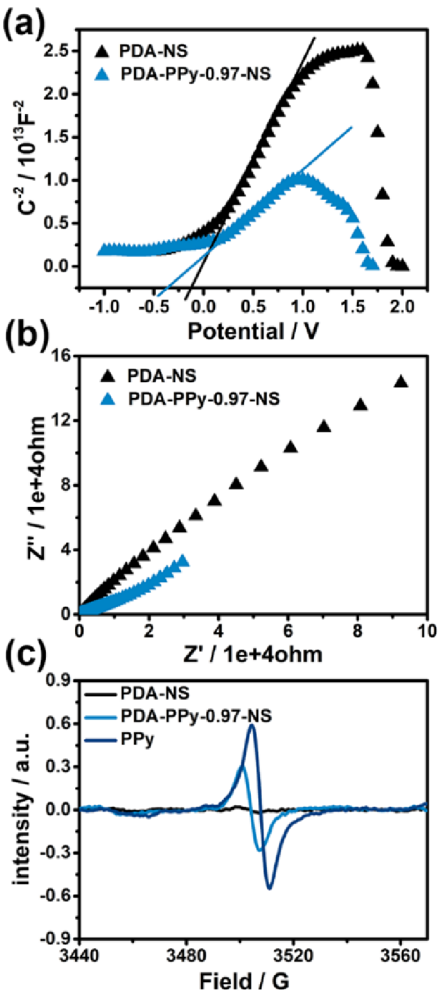

Figure 5. (a) MS plots, (b) EIS, and (c) EPR spectra of PDA-NS and PDA-PPy-0.97-NS.

absorbing nanomaterials.[33,36] As shown in Figure 6b, TAS for both Cy5 and Cy5/PDA-PPy-0.97-NS were negative at 650 nm, which revealed a possible quenching mechanism of the ground state bleach (GSB).[16] As the delay time increased from 2.08 to 1089.58 ps, the GSB signal at 650 nm showed an obvious decrease. The lifetimes of the dynamic processes of Cy5 and Cy5/PDA-PPy-0.97-NS complexes were fitted in terms of three single exponentials of τ_1, τ_2, and τ_3 (Figure 6c,d). In contrast to the photoexcited carrier dynamics of Cy5 (τ_1 = 18.29 ps, τ_2 = 495.95 ps, and τ_3 = 871.41 ps) at 650 nm, the Cy5/PDA-PPy-0.97-NS presented shorter decay dynamic responses (τ_1 = 0.11 ps, τ_2 = 52.10 ps, and τ_3 = 865.85 ps). The PET from the excited state of Cy5 to PDA-PPy-0.97-NS, which in turn accelerated GSB signal recovery,[37,38] might have contributed to the shortened lifetimes of Cy5/PDA-PPy-0.97-NS complexes. As shown in Figure 6d, the process occurring at 52.1 ps (τ_2) should be assigned to the deactivation of the singlet excited state (S_1) to the ground state (S_0).[39] The process at 0.11 ps (τ_1) was most likely assigned to the electron injection from the S_1 state of Cy5 to the PDA-PPy-0.97-NS.

The PET process between Cy5 and PDA-PPy-0.97-NS is then depicted in Figure 6e. The calculated energy diagram demonstrated that the LUMO/HOMO of Cy5 was −2.77/−4.93 eV vs vacuum, which was aligned and coupled with the energy levels of PDA-PPy-0.97-NS (−4.74/−5.03 eV vs vacuum). Excited by light, electrons in the HOMO of Cy5 could switch from the ground state to the excited state. Since the LUMO energy level of PDA-PPy-0.97-NS was between the LUMO and HOMO energy levels of the Cy5 fluorophore, the excited state of the fluorophore was able to donate electrons to the LUMO of PDA-PPy-0.97-NS. The electrons transferred from the LUMO of Cy5 to the LUMO of PDA-PPy-NS therefore could prevent the return of electrons in the LUMO, leading to fluorescence quenching. This process can be characterized as the donor-excited PET process (d-PET), in which the fluorophore itself serves as an electron donor.[40,41]

The fluorescence quenching kinetics were then investigated ahead of miRNA detection. Figure 7a−d shows the fluorescence decay kinetics curves of the ssDNA probe and ssDNA-miRNA heteroduplex (dsDNA) in the presence of four kinds of nanosheets. After the addition of PDA-NS, a gradual decrease in the fluorescence intensity of the ssDNA probe was observed within 400 s, but the quenching efficiency (QE) only reached 41.97% at 100 s (Figure 7a). However, after the addition of PDA-PPy-0.39-NS, PDA-PPy-0.68-NS, and PDA-PPy-0.97-NS, the fluorescence intensity of the ssDNA probe decreased fairly fast within 100 s, with the QE reaching 92.9%, 97.2%, and 99.4%, respectively (Figure 7b−d), which should be attributed to the strong absorption by the $\pi-\pi$ stacking and PET[34,42] between Cy5-ssDNA and PDA-PPy-NS. It is also of note that the fluorescence of the ds complex was mostly quenched at the fast decay stage (50 s, Figure 7a−d). The difference in affinity of nanosheets toward ds and ss nucleotides was next evaluated by calculating the fluorescence intensity ratio of dsDNA and ssDNA probes (F_{ds}/F_{ss}). While the F_{ds}/F_{ss} ratio of the PDA-NS showed a negligible change, F_{ds}/F_{ss} ratios of PDA-PPy-0.39-NS and PDA-PPy-0.68-NS gradually increased over time. The fluorescence quenching ability of various nanosheets toward the ssDNA probe was further visualized by confocal laser scanning microscope (CLSM) images (Figure 7e) of the suspensions after incubating for 400 s, where the discrepancy was similar to the results shown in Figure 7a−d. At this time point, PDA-PPy-0.97-NS possessed the largest F_{ds}/F_{ss} ratio of ∼41, indicating the most significant difference in the affinity (Figure 7f) of nanosheets toward ssDNA and dsDNA.

Subsequently, fluorescence quenching abilities of nanosheets with various concentrations toward ssDNA were investigated by using a sufficiently long time (30 min) of incubation to reach the equilibrium. As presented in Figure 8a, for all nanosheets, the QE of the 50 nM Cy5-ssDNA probe increased greatly along with an increase in the concentration. When the concentration of nanosheets reached 10 μg mL^{-1}, the QE of PDA-PPy-0.97-NS was up to 99.59%, which was 35.44% higher than PDA-NS (64.15%). The mass ratio of the ssDNA probe/nanoquencher under the complete quenching condition was 36.9 (PDA-PPy-0.97-NS), which was remarkably higher than those of PPy (7.4) and PDA nanomaterials (4.1) in previous studies[43,44] and even comparable to that of graphene oxide (GO) (14.7−40.9, Table S2).[45,46] Overall, these results again confirm that the surface of PPy−PDA composite nanosheets has high affinity toward ssDNA probes. In light of the fact that the major change in the sensing surface for the nanoquencher after PPy hybridization was the generation of these PPy islands, the high affinity and strong PET between the PPy islands in PDA-PPy-NS and the dyes in the ssDNA probe might be the reason accounting for the significant increase in QE. Next, quenching curves (Figure S4) by using FAM (6-carboxyfluorescein, Ex 480 nm, Em 520 nm) and

https://doi.org/10.1021/acsami.1c11301
ACS Appl. Mater. Interfaces XXXX, XXX, XXX−XXX

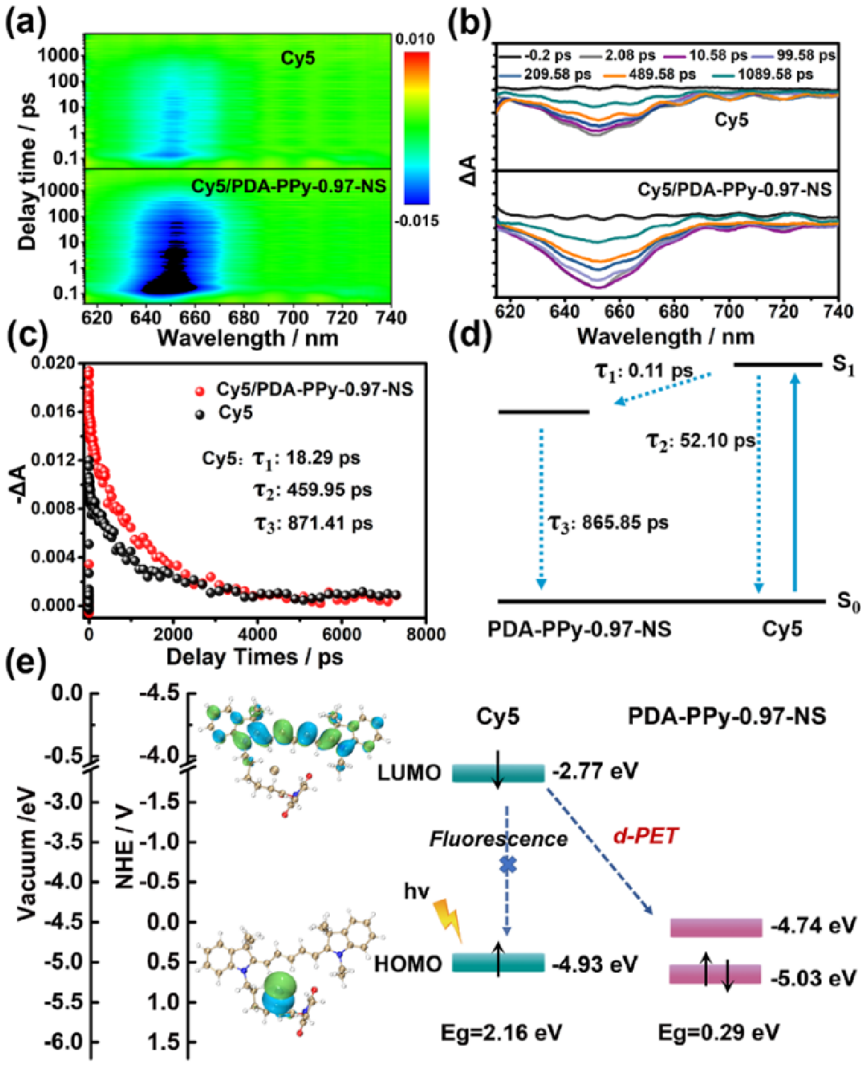

Figure 6. (a) 2D map of time-resolved TAS for Cy5 (top) and Cy5/PDA-PPy-0.97-NS (bottom) under 645 nm wavelength pump laser excitation; (b) TAS of Cy5 and Cy5/PDA-PPy-0.97-NS complexes at various probe delays; and (c) photoexcited carrier dynamics of Cy5 and Cy5/PDA-PPy-0.97-NS at a probe wavelength of 650 nm; both decay curves are fitted to a triple exponential function; (d) schematic representation of photophysical processes in Cy5/PDA-PPy-0.97-NS complexes; and (e) schematic diagram of energy level band gaps of Cy5 and PDA-PPy-0.97-NS along with the PET quenching process. The inset shows the simulated MO diagrams of the Cy5 molecule.

TAMRA (6-carboxytetramethylrhodamine, Ex 542 nm, Em 582 nm) as supplementary dyes of Cy5 (Ex 645 nm and Em 665 nm) were obtained and the results revealed comparable ssDNA/nanoquencher mass ratios (36.1 for FAM and 45.6 for TAMRA) under the complete quenching condition. As known, typical organic or inorganic semiconductors have EAs (the energy difference between the vacuum level and the LUMO/conduction band minimum level) and IEs (the energy difference between the vacuum level and the HOMO/valence band maximum level) in the range of 2−4 and 4.5−6.5 eV,[47] respectively. Considering the calculated values of the LUMO/HOMO energy levels at −4.74/−5.03 eV vs vacuum (0.24/0.53 V vs NHE) for PDA-PPy-NS, the band alignment by the straddling gap or staggered gap could be generally formed between this nanoquencher and common organic dyes. This might be the factor contributing to the strong quenching ability of dyes over a wide range of emission wavelengths.

By measuring the ratio (F/F_0) of fluorescence for nanoquencher−probe suspensions (10 μg mL^{-1}, 50 nM) in the presence/absence of miRNA with a sufficiently high concentration (100 nM), the detection conditions including temperature, pH, and salt concentration were optimized to achieve the best sensing performance. As shown in Figure 8b, maximum F/F_0 values were obtained at intermediate temperatures of 37/45 °C, possibly because higher or lower temperatures are not thermodynamically beneficial for the formation of DNA/miRNA heteroduplexes. Optimized pH/salt concentrations at pH 7.4/100 mM NaCl were also observed (Figure 8c,d), which might be related to the appropriate attraction/repulsion interactions[44] among the probe, RNA, and nanoquenchers under these conditions.

MicroRNA-21 (miR-21) is a widely expressed miRNA in mammalian cells, whose upregulation has been shown to be in association with several types of cancer.[48] Here, we tried to evaluate the sensitivity of our systems by taking miR-21 as a model analyte. Considering the low quenching ability of PDA-NS (Figure S5), the nanoquencher concentration of PDA-NS was set as 40 μg mL^{-1} to meet the requirements of complete quenching conditions for the DNA probe. Along with the concentrations of miRNA-21 increasing from 0 to 100 nM, the

https://doi.org/10.1021/acsami.1c11301
ACS Appl. Mater. Interfaces XXXX, XXX, XXX−XXX

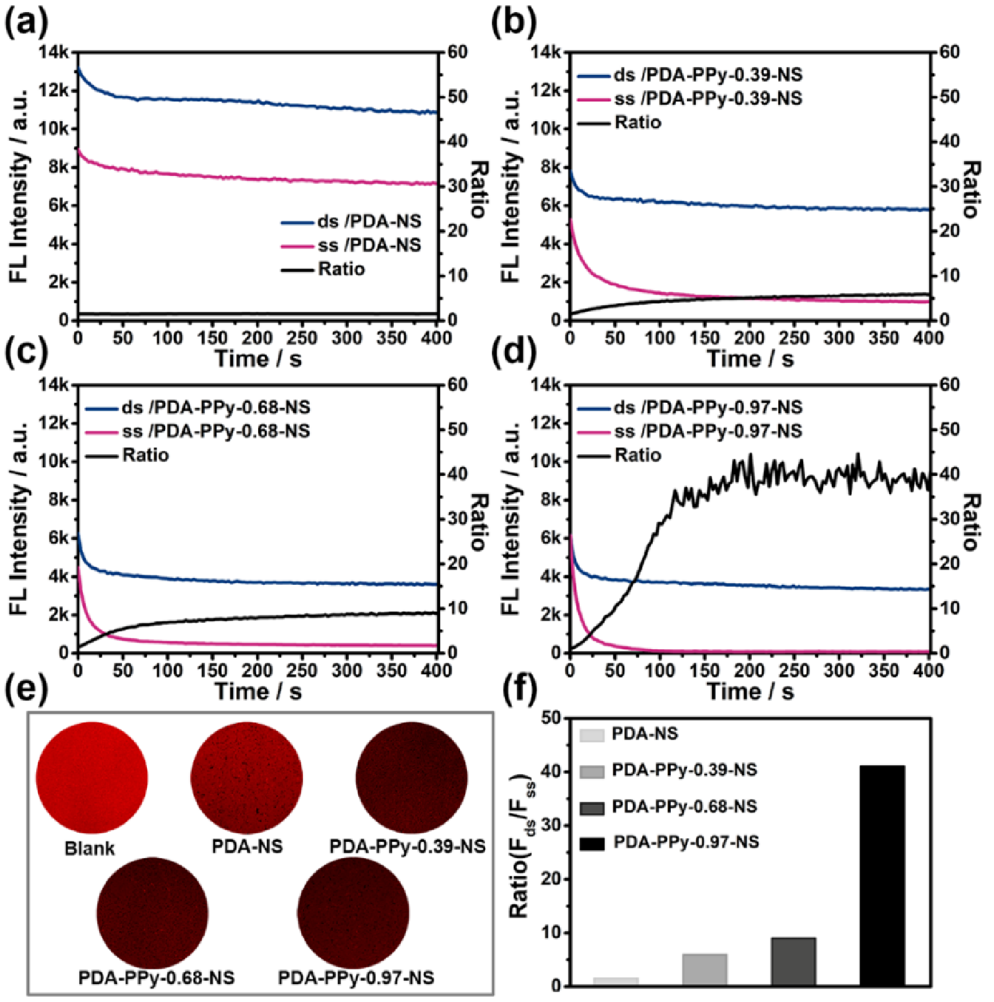

Figure 7. (a–d) Fluorescence quenching kinetics of nanosheets (10 μg mL^{-1}) toward the 50 nM Cy5 labeled ss DNA probe (red line) and ds probe-miRNA heteroduplex (blue line) and fluorescence intensity ratios (black line) of ds and ss oligonucleotides from the red and blue lines: (a) PDA-NS, (b) PDA-PPy-0.39-NS, (c) PDA-PPy-0.68-NS, and (d) PDA-PPy-0.97-NS; (e) CLSM images for visible comparison of the fluorescence change by incubating suspensions of various nanosheets with Cy5-ssDNA probe solution for 400 s; and (f) fluorescence intensity ratios (F_{ds}/F_{ss}) in the presence of nanosheets (10 μg mL^{-1}).

fluorescence intensities of both PDA-NS and PDA-PPy-0.97-NS sensing platforms displayed a progressive increase (Figure 9a,b). As shown in Figure 9c,d, the signal intensity of the PDA-NS sensor was linearly positively correlated with the target concentrations ranging from 0.02 to 0.5 nM (Figure 9c). The calibration equation is $F = 348.5C + 246.16$ (the correlation coefficient R^2 was 0.9924), where F indicates the fluorescence intensity and C indicates the concentration of miR-21. The limit of detection (LOD) was thereby calculated to be 172.3 pM based on the 3σ rule. On the other hand, the PDA-PPy-0.97-NS biosensor showed a linear relationship ranging from 0.005 to 0.1 nM ($F = 1747.4C + 113.95$, $R^2 = 0.9923$, Figure 9d). The LOD of the PDA-PPy-0.97-NS biosensor was calculated to be 23.1 pM. Compared with the PDA-NS biosensor, the LOD of PDA-PPy-0.97-NS was reduced by about 6.5 times. It should be noted that the LOD of PDA-PPy-0.97-NS was lower than those of the previously reported biosensors based on PDA and GO nanoquenchers (Table S2).[44−46] This excellent sensitivity should mainly depend on the high fluorescence quenching ability of PDA-PPy-0.97-NS, which is attributed to the efficient PET between nanosheets with a narrow band gap and Cy5-ssDNA.

Next, the specificity of miR-21 detection was investigated by selecting miR-21 analogues, including those with single-mismatched base (SM-miR-21), double-mismatched bases (DM-miR-21), and triple-mismatched bases (TM-miR-21). Two other tumor-related miRNAs (miR-141 and let-7a) were chosen as competing targets of miR-21 (base sequences are listed in detail in Table S1). Whatever the fluorescent quencher was utilized, PDA-NS or PDA-PPy-0.97-NS, the fluorescence intensity ratio (F/F_0) of target miR-21 was significantly higher than those of other mismatched bases at the same concentration (Figure 10a,b). Noteworthily, for the PDA-PPy-0.97-NS-based biosensor, the value of F/F_0 of miR-21 was 4.4 and 6.2 times higher than those of SM-miR-21 and DM-miR-21, respectively, which was equivalent to that obtained from the PDA-NS nanosensor (4.8 and 6.5 times). Meanwhile, F/F_0 values gradually dropped with the increase of mismatched bases and were even lower when it came to miR-141 and let-7a. Taken together, these results indicate that the PDA-PPy-0.97-NS-based fluorescent biosensor can offer superior selectivity to distinguish highly homologous sequences of miRNA families with single-base mismatches.

The repeated tests by measuring the fluorescence intensity for 10 batches of nanoquencher samples toward 100 nM

https://doi.org/10.1021/acsami.1c11301
ACS Appl. Mater. Interfaces XXXX, XXX, XXX−XXX

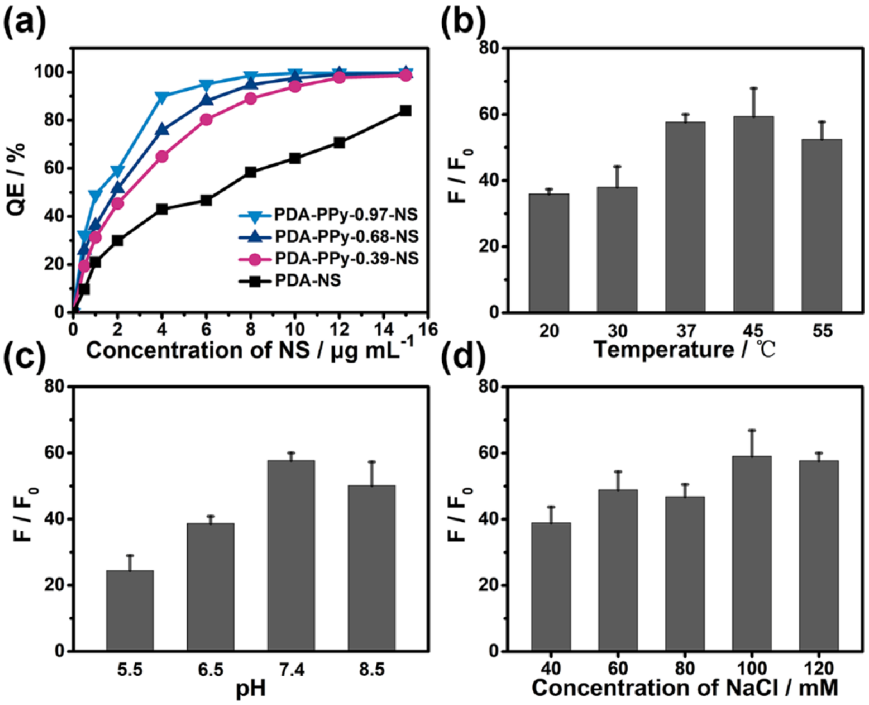

Figure 8. (a) QE of the 50 nM Cy5-ssDNA probe by different concentrations (0−15 μg mL^{-1}) of nanosheets. (b−d) Optimization of detection parameters by measuring the ratio (F/F_0) of fluorescence for nanoquencher−probe suspensions (10 μg mL^{-1}, 50 nM) in the presence/absence of 100 nM miRNA under different experiments conditions: (b) temperatures, (c) pH value, and (d) concentrations of NaCl. Error bars are the standard deviation of three repetitive experiments.

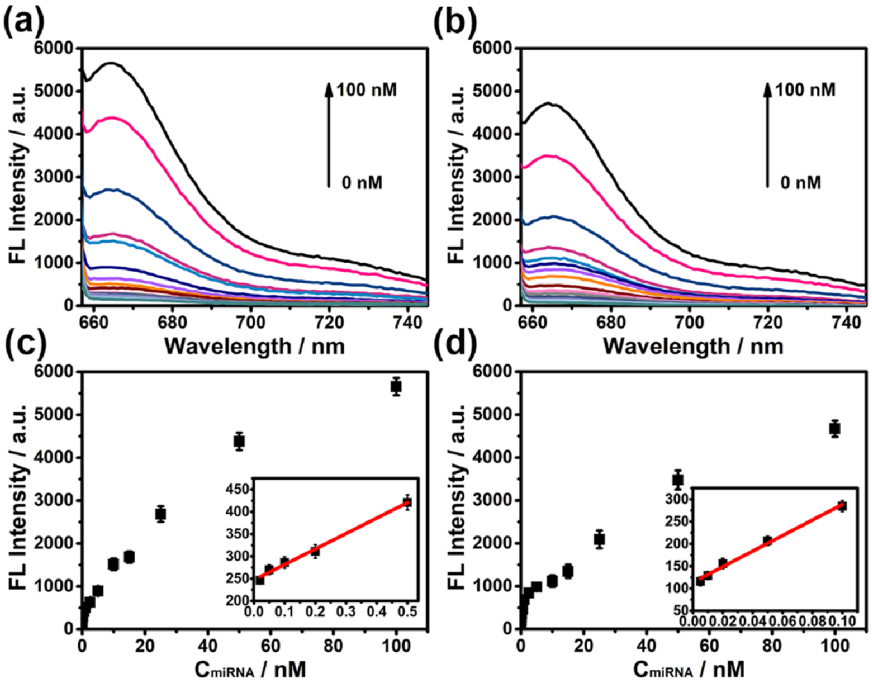

Figure 9. (a and b) Fluorescence emission spectra of the Cy5-ssDNA probe (50 nM) and nanosheets vs miRNA-21 concentrations (0.005, 0.01, 0.02, 0.05, 0.1, 0.2, 0.5, 1, 2.5, 5, 10, 15, 25, 50, and 100 nM): (a) PDA-NS (40 μg mL^{-1}) and (b) PDA-PPy-0.97-NS (10 μg mL^{-1}); (c and d) fluorescence peak intensities at 665 nm of the Cy5-ssDNA probe (50 nM) and nanosheets vs miRNA-21 concentrations: (c) PDA-NS and (d) PDA-PPy-0.97-NS. The insets show calibration curves of the fluorescence (FL) intensity vs target concentration. Error bars represent the standard deviation of three independent measurements.

miRNA showed a low relative standard deviation value of 2.10% (Figure S6), indicating the high stability of the detection. To investigate the applicability of the PDA-PPy-NS nanosensor for realistic miRNA analysis, a proof-of-concept detection experiment was first carried out by using samples through adding different amounts of miRNA in fetal bovine serum (10% in PBS, pH 7.4), which is a widely applied model matrix to realize the simulation of biological samples. As

https://doi.org/10.1021/acsami.1c11301
ACS Appl. Mater. Interfaces XXXX, XXX, XXX−XXX

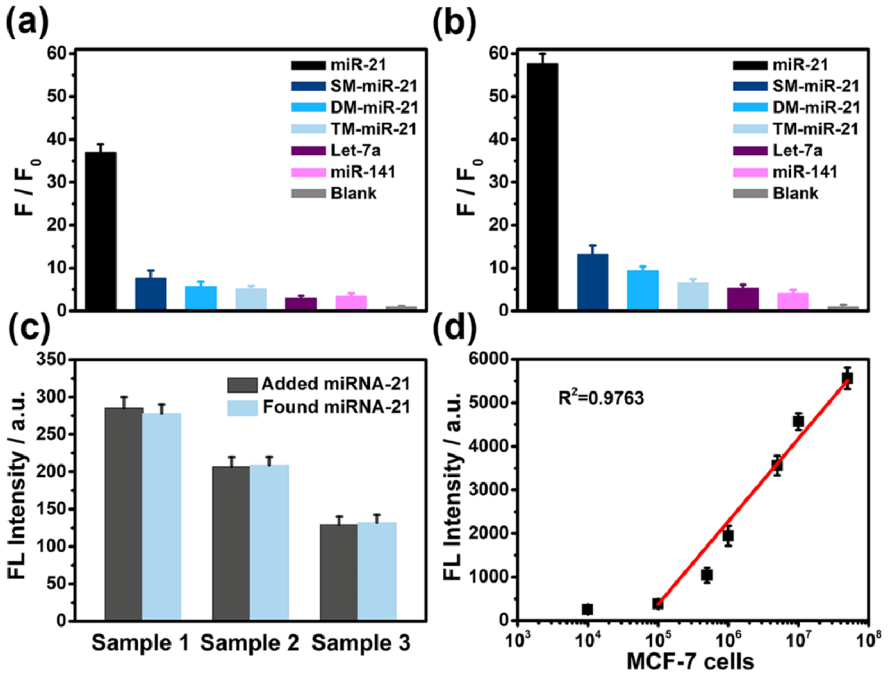

Figure 10. Specificity of detection systems by measuring the F/F_0 ratios of (a) PDA-NS and (b) PDA-PPy-0.97-NS in the presence of target miRNA-21 and miRNAs (100 nM) with various mismatched bases. SM/DM/TM-miRNA-21, let-7a and miRNA-141 represent miRNAs with single/double/triple base and multibase mismatches, respectively. (c) Detection of miRNA-21 with standard concentrations (0.1, 0.05, and 0.01 nM) in fetal bovine serum (10% in PBS, pH 7.4). (d) Detection of miRNA-21 in total RNA samples from MCF-7 cell lines. Error bars represent the standard deviation of three independent measurements.

shown in Figure 10c, the analytical recoveries from solutions with different levels of added miRNA were between 93.9% and 108.8%. Moreover, miRNA from the total RNA samples of cell lysate for a tumor cell line (MCF-7 with a high abundance of upregulated miRNA-21) can also be detected (Figure 10d) when the cell number is above 10^4. The above results are satisfactory, illustrating the great potential of the nano-quencher-based biosensors for real samples.

4. CONCLUSIONS

In conclusion, we have successfully developed two-dimensional π-conjugated polymer nanomaterials (PDA-PPy-NS) through an interfacial composite between PDA and π-electron-rich molecules, i.e., nucleic acid and PPy. By this means, PDA-PPy-NS can possess unique π electronic coupling and π planar stacking structures, providing new design methods for constructing two-dimensional nanomaterials with a narrow band gap (0.29 eV) and high PET efficiency. More importantly, we further validate that the fluorescence quenching ability of PDA-PPy-NS can be enhanced by the high PET efficiency, which is comparable to that achieved by GO. The PDA-PPy-NS-based biosensor has been therefore used for the detection of miRNA-21 and found to have a low LOD (23.1 pM) and high selectivity. Taken together, our findings offer a novel route to the construction of a high-performance sensing platform.

■ ASSOCIATED CONTENT

Supporting Information

The Supporting Information is available free of charge at https://pubs.acs.org/doi/10.1021/acsami.1c11301.

Experimental section; instruments; characterizations; and supplementary results on surface roughness from AFM images; TEM image of PPy nanoparticles; absorption and fluorescence spectra; comparison of detection performance; quenching efficiencies; repeatability, etc. (PDF)

■ AUTHOR INFORMATION

Corresponding Authors

Lu Wang − *Key Laboratory of Biorheological Science and Technology, Ministry of Education, College of Bioengineering, Chongqing University, Chongqing 400044, China;* orcid.org/0000-0002-4614-4427; Email: wanglu622@cqu.edu.cn

Jixi Zhang − *Key Laboratory of Biorheological Science and Technology, Ministry of Education, College of Bioengineering, Chongqing University, Chongqing 400044, China;* orcid.org/0000-0003-3460-0867; Email: jixizhang@cqu.edu.cn

Authors

Mengnan Yang − *Key Laboratory of Biorheological Science and Technology, Ministry of Education, College of Bioengineering, Chongqing University, Chongqing 400044, China*

Zhenqiang Wang − *Key Laboratory of Biorheological Science and Technology, Ministry of Education, College of Bioengineering, Chongqing University, Chongqing 400044, China*

Tao Ding − *Key Laboratory of Biorheological Science and Technology, Ministry of Education, College of Bioengineering, Chongqing University, Chongqing 400044, China*

Jia Tang − *Key Laboratory of Biorheological Science and Technology, Ministry of Education, College of Bioengineering, Chongqing University, Chongqing 400044, China*

https://doi.org/10.1021/acsami.1c11301
ACS Appl. Mater. Interfaces XXXX, XXX, XXX−XXX

Xiyue Xie − *Key Laboratory of Biorheological Science and Technology, Ministry of Education, College of Bioengineering, Chongqing University, Chongqing 400044, China*
Yuxin Xing − *Key Laboratory of Biorheological Science and Technology, Ministry of Education, College of Bioengineering, Chongqing University, Chongqing 400044, China*
Kaiyong Cai − *Key Laboratory of Biorheological Science and Technology, Ministry of Education, College of Bioengineering, Chongqing University, Chongqing 400044, China;* orcid.org/0000-0001-9029-680X

Complete contact information is available at: https://pubs.acs.org/10.1021/acsami.1c11301

Notes

The authors declare no competing financial interest.

■ ACKNOWLEDGMENTS

This work was supported in part by the National Natural Science Foundation of China (NSFC, Grant nos. 51773022, 21734002, and 51825302), Project supported by Graduate Scientific Research, and Innovation Foundation of Chongqing, China (Grant no. CYB20068). The Analytical and Testing Center of Chongqing University is greatly acknowledged for the help with the characterization of materials. The worker Liang Yan from Shiyanjia Lab (www.shiyanjia.com) is greatly acknowledged for the assistance with TAS measurements.

■ REFERENCES

(1) Gebert, L. F. R.; MacRae, I. J. Regulation of MicroRNA Function in animals. *Nat. Rev. Mol. Cell Biol.* **2019**, *20*, 21−37.
(2) Hill, M.; Tran, N. MicroRNAs Regulating MicroRNAs in Cancer. *Trends Cancer* **2018**, *4*, 465−468.
(3) Kilic, T.; Erdem, A.; Ozsoz, M.; Carrara, S. MicroRNA Biosensors: Opportunities and Challenges among Conventional and Commercially Available Techniques. *Biosens. Bioelectron.* **2018**, *99*, 525−546.
(4) Zhang, J.; Lan, T.; Lu, Y. Molecular Engineering of Functional Nucleic Acid Nanomaterials toward In Vivo Applications. *Adv. Healthcare Mater.* **2019**, *8*, No. 1801158.
(5) Xiao, M.; Lai, W.; Man, T.; Chang, B.; Li, L.; Chandrasekaran, A. R.; Pei, H. Rationally Engineered Nucleic Acid Architectures for Biosensing Applications. *Chem. Rev.* **2019**, *119*, 11631−11717.
(6) Wang, Z.-Y.; Li, P.; Cui, L.; Qiu, J.-G.; Jiang, B.; Zhang, C.-Y. Integration of Nanomaterials with Nucleic Acid Amplification Approaches for Biosensing. *Trends Anal. Chem.* **2020**, *129*, No. 115959.
(7) Xu, W.; He, W.; Du, Z.; Zhu, L.; Huang, K.; Lu, Y.; Luo, Y. Functional Nucleic Acid Nanomaterials: Development, Properties, and Applications. *Angew. Chem., Int. Ed.* **2021**, *60*, 6890−6918.
(8) Chen, Y.; Wu, Y.; Sun, B.; Liu, S.; Liu, H. Two-Dimensional Nanomaterials for Cancer Nanotheranostics. *Small* **2017**, *13*, No. 1603446.
(9) Hu, Z.; Suo, Z.; Liu, W.; Zhao, B.; Xing, F.; Zhang, Y.; Feng, L. DNA Conformational Polymorphism for Biosensing Applications. *Biosens. Bioelectron.* **2019**, *131*, 237−249.
(10) MacFarlane, L. R.; Shaikh, H.; Garcia-Hernandez, J. D.; Vespa, M.; Fukui, T.; Manners, I. Functional Nanoparticles through π-Conjugated Polymer Self-Assembly. *Nat. Rev. Mater.* **2021**, *6*, 7−26.
(11) Xie, X.; Tang, J.; Xing, Y.; Wang, Z.; Ding, T.; Zhang, J.; Cai, K. Intervention of Polydopamine Assembly and Adhesion on Nanoscale Interfaces: State-of-the-Art Designs and Biomedical Applications. *Adv. Healthcare Mater.* **2021**, *10*, No. 2002138.
(12) Chen, Y.; Wang, C. Designing High Performance Organic Batteries. *Acc. Chem. Res.* **2020**, *53*, 2636−2647.
(13) Liu, C.; Wang, K.; Gong, X.; Heeger, A. J. Low Bandgap Semiconducting Polymers for Polymeric Photovoltaics. *Chem. Soc. Rev.* **2016**, *45*, 4825−4846.
(14) Ying, L.; Huang, F.; Bazan, G. C. Regioregular Narrow-Bandgap-Conjugated Polymers for Plastic Electronics. *Nat. Commun.* **2017**, *8*, No. 14047.
(15) Zhang, J.; Yang, C.; Zhang, R.; Chen, R.; Zhang, Z.; Zhang, W.; Peng, S.-H.; Chen, X.; Liu, G.; Hsu, C.-S.; Lee, C.-S. Biocompatible D−A Semiconducting Polymer Nanoparticle with Light-Harvesting Unit for Highly Effective Photoacoustic Imaging Guided Photothermal Therapy. *Adv. Funct. Mater.* **2017**, *27*, No. 1605094.
(16) Cao, Y.; Dou, J.-H.; Zhao, N.-J.; Zhang, S.; Zheng, Y.-Q.; Zhang, J.-P.; Wang, J.-Y.; Pei, J.; Wang, Y. Highly Efficient NIR-II Photothermal Conversion Based on an Organic Conjugated Polymer. *Chem. Mater.* **2017**, *29*, 718−725.
(17) Zhang, J.; Chen, J.; Ren, J.; Guo, W.; Li, X.; Chen, R.; Chelora, J.; Cui, X.; Wan, Y.; Liang, X.-J.; Hao, Y.; Lee, C.-S. Biocompatible Semiconducting Polymer Nanoparticles as Robust Photoacoustic and Photothermal Agents Revealing the Effects of Chemical Structure on High Photothermal Conversion Efficiency. *Biomaterials* **2018**, *181*, 92−102.
(18) Lyu, Y.; Fang, Y.; Miao, Q.; Zhen, X.; Ding, D.; Pu, K. Intraparticle Molecular Orbital Engineering of Semiconducting Polymer Nanoparticles as Amplified Theranostics for In Vivo Photoacoustic Imaging and Photothermal Therapy. *ACS Nano* **2016**, *10*, 4472−4481.
(19) Lin, Q.; Yang, Y.; Ma, Y.; Zhang, R.; Wang, J.; Chen, X.; Shao, Z. Bandgap Engineered Polypyrrole−Polydopamine Hybrid with Intrinsic Raman and Photoacoustic Imaging Contrasts. *Nano Lett.* **2018**, *18*, 7485−7493.
(20) Liu, Y.; Huang, Y.; Duan, X. Van Der Waals Integration before and beyond Two-Dimensional Materials. *Nature* **2019**, *567*, 323−333.
(21) Ding, T.; Xing, Y.; Wang, Z.; Guan, H.; Wang, L.; Zhang, J.; Cai, K. Structural Complementarity from DNA for Directing Two-Dimensional Polydopamine Nanomaterials with Biomedical Applications. *Nanoscale Horiz.* **2019**, *4*, 652−657.
(22) Guan, H.; Ding, T.; Zhou, W.; Wang, Z.; Zhang, J.; Cai, K. Hexagonal Polypyrrole Nanosheets from Interface Driven Heterogeneous Hybridization and Self-Assembly for Photothermal Cancer Treatment. *Chem. Commun.* **2019**, *55*, 4359−4362.
(23) Huang, J.; Wang, S.; Xing, Y.; Zhou, W.; Zhang, J.; Cai, K. Interface-Hybridization-Enhanced Photothermal Performance of Polypyrrole/Polydopamine Heterojunctions on Porous Nanoparticles. *Macromol. Rapid Commun.* **2019**, *40*, No. 1900263.
(24) Inoue, F.; Ando, R. A.; Izumi, C. M. S.; Corio, P. Spectroscopic Characterization of Carbon Nanotube-Polypyrrole Composites. *J. Phys. Chem. C* **2014**, *118*, 18240−18248.
(25) Steckler, T. T.; Zhang, X.; Hwang, J.; Honeyager, R.; Ohira, S.; Zhang, X.-H.; Grant, A.; Ellinger, S.; Odom, S. A.; Sweat, D.; Tanner, D. B.; Rinzler, A. G.; Barlow, S.; Brédas, J.-L.; Kippelen, B.; Marder, S. R.; Reynolds, J. R. A Spray-Processable, Low Bandgap, and Ambipolar Donor−Acceptor Conjugated Polymer. *J. Am. Chem. Soc.* **2009**, *131*, 2824−2826.
(26) Marchioni, F.; Yang, J.; Walker, W.; Wudl, F. A Low Band Gap Conjugated Polymer for Supercapacitor Devices. *J. Phys. Chem. B* **2006**, *110*, 22202−22206.
(27) Costa, J. C. S.; Taveira, R. J. S.; Lima, C. F. R. A. C.; Mendes, A.; Santos, L. M. N. B. F. Optical Band Gaps of Organic Semiconductor Materials. *Opt. Mater.* **2016**, *58*, 51−60.
(28) Majhi, D.; Das, K.; Mishra, A.; Dhiman, R.; Mishra, B. G. One Pot Synthesis of CdS/BiOBr/$Bi_2O_2CO_3$: A Novel Ternary Double Z-Scheme Heterostructure Photocatalyst for Efficient Degradation of Atrazine. *Appl. Catal., B* **2020**, *260*, No. 118222.
(29) Cao, X.; Wang, Y.; Lin, J.; Ding, Y. Ultrathin CoO_x Nanolayers Derived from Polyoxometalate for Enhanced Photoelectrochemical of Hematite Photoanodes. *J. Mater. Chem. A* **2019**, *7*, 6294−6303.
(30) He, B.; Jia, S.; Zhao, M.; Wang, Y.; Chen, T.; Zhao, S.; Li, Z.; Lin, Z.; Zhao, Y.; Liu, X. General and Robust Photothermal-Heating-

Enabled High-Efficiency Photoelectrochemical Water Splitting. *Adv. Mater.* **2021**, *33*, No. 2004406.
(31) Li, Y.; Wang, W.; Zhang, B.; Fu, L.; Wan, M.; Li, G.; Cai, Z.; Tu, S.; Duan, X.; Seh, Z. W.; Jiang, J.; Sun, Y. Manipulating Redox Kinetics of Sulfur Species Using Mott−Schottky Electrocatalysts for Advanced Lithium-Sulfur Batteries. *Nano Lett.* **2021**, *21*, 6656−6663.
(32) Wang, Y.; Zhu, W.; Du, W.; Liu, X.; Zhang, X.; Dong, H.; Hu, W. Cocrystals Strategy Towards Materials for Near-Infrared Photothermal Conversion and Imaging. *Angew. Chem., Int. Ed.* **2018**, *57*, 3963−3967.
(33) Xue, T.; Bongu, S. R.; Huang, H.; Liang, W.; Wang, Y.; Zhang, F.; Liu, Z.; Zhang, Y.; Zhang, H.; Cui, X. Ultrasensitive Detection of MicroRNA Using a Bismuthene-Enabled Fluorescence Quenching Biosensor. *Chem. Commun.* **2020**, *56*, 7041−7044.
(34) Qiang, W.; Li, W.; Li, X.; Chen, X.; Xu, D. Bioinspired Polydopamine Nanospheres: A Superquencher for Fluorescence Sensing of Biomolecules. *Chem. Sci.* **2014**, *5*, 3018−3024.
(35) Fan, D.; Zhu, X.; Zhai, Q.; Wang, E.; Dong, S. Polydopamine Nanotubes as an Effective Fluorescent Quencher for Highly Sensitive and Selective Detection of Biomolecules Assisted with Exonuclease III Amplification. *Anal. Chem.* **2016**, *88*, 9158−9165.
(36) Dini, D.; Calvete, M. J. F.; Hanack, M. Nonlinear Optical Materials for the Smart Filtering of Optical Radiation. *Chem. Rev.* **2016**, *116*, 13043−13233.
(37) Kim, S.-Y.; Cho, Y.-J.; Son, H.-J.; Cho, D. W.; Kang, S. O. Photoinduced Electron Transfer in a Bodipy-Ortho-Carborane Dyad Investigated by Time-Resolved Transient Absorption Spectroscopy. *J. Phys. Chem. A* **2018**, *122*, 3391−3397.
(38) Ghosh, A.; Ghosh, S.; Jana, B.; Patra, A. Ultrafast Relaxation Processes of Conjugated Polymer Nanoparticles in Presence of Au Nanoparticles. *Chem. Asian J.* **2019**, *14*, 4681−4687.
(39) Xiong, W.; Du, L.; Lo, K. C.; Shi, H.; Takaya, T.; Iwata, K.; Chan, W. K.; Phillips, D. L. Control of Electron Flow Direction in Photoexcited Cycloplatinated Complex Containing Conjugated Polymer−Single-Walled Carbon Nanotube Hybrids. *J. Phys. Chem. Lett.* **2018**, *9*, 3819−3824.
(40) Sun, W.; Li, M.; Fan, J.; Peng, X. Activity-Based Sensing and Theranostic Probes Based on Photoinduced Electron Transfer. *Acc. Chem. Res.* **2019**, *52*, 2818−2831.
(41) Ueno, T.; Urano, Y.; Setsukinai, K.-I.; Takakusa, H.; Kojima, H.; Kikuchi, K.; Ohkubo, K.; Fukuzumi, S.; Nagano, T. Rational Principles for Modulating Fluorescence Properties of Fluorescein. *J. Am. Chem. Soc.* **2004**, *126*, 14079−14085.
(42) Zou, H. Y.; Gao, P. F.; Gao, M. X.; Huang, C. Z. Polydopamine-Embedded $Cu_{2-X}Se$ Nanoparticles as a Sensitive Biosensing Platform through the Coupling of Nanometal Surface Energy Transfer and Photo-Induced Electron Transfer. *Analyst* **2015**, *140*, 4121−4129.
(43) Ke, K.; Lin, L.; Liang, H.; Chen, X.; Han, C.; Li, J.; Yang, H.-H. Polypyrrole Nanoprobes with Low Non-Specific Protein Adsorption for Intracellular MRNA Detection and Photothermal Therapy. *Chem. Commun.* **2015**, *51*, 6800−6803.
(44) Wang, Z.; Zhang, J.; Chen, F.; Cai, K. Fluorescent MiRNA Analysis Enhanced by Mesopore Effects of Polydopamine Nanoquenchers. *Analyst* **2017**, *142*, 2796−2804.
(45) Pan, W.; Liu, B.; Gao, X.; Yu, Z.; Liu, X.; Li, N.; Tang, B. A Graphene-Based Fluorescent Nanoprobe for Simultaneous Monitoring of MiRNA and MRNA in Living Cells. *Nanoscale* **2018**, *10*, 14264−14271.
(46) Li, F.; Pei, H.; Wang, L.; Lu, J.; Gao, J.; Jiang, B.; Zhao, X.; Fan, C. Nanomaterial-Based Fluorescent DNA Analysis: A Comparative Study of the Quenching Effects of Graphene Oxide, Carbon Nanotubes, and Gold Nanoparticles. *Adv. Funct. Mater.* **2013**, *23*, 4140−4148.
(47) Kahn, A. Fermi Level, Work Function and Vacuum Level. *Mater. Horiz.* **2016**, *3*, 7−10.
(48) Oudeng, G.; Au, M.; Shi, J.; Wen, C.; Yang, M. One-Step in Situ Detection of MiRNA-21 Expression in Single Cancer Cells Based on Biofunctionalized MoS_2 Nanosheets. *ACS Appl. Mater. Interfaces* **2018**, *10*, 350−360.

https://doi.org/10.1021/acsami.1c11301
ACS Appl. Mater. Interfaces XXXX, XXX, XXX−XXX